Electronic Supplementary Material (ESI) for Materials Horizons.
This journal is © The Royal Society of Chemistry 2023

Gradient Heating Induced Better Balance Between Water Transportation, Salt resistance and Heat Supply in a High Performance Multi-functional Solar-thermal Desalination Device

Chuanliang Chen, Lianhu Xiong, Xuezhong Zhang, Ke Tian, Zijian Dai, Qiang Fu, Hua Deng*

College of Polymer Science and Engineering, State Key Laboratory of Polymer Materials Engineering, Sichuan University, Chengdu, 610065, China

*: Corresponding author: Hua Deng

E-mail: huadeng@scu.edu.cn (H. Deng), Tel.: + 86-28-85460953

Experimental section

Materials

Multiwalled Carbon nanotubes (CNT, NC-7000) with diameters of 10 nm and carbon purity of 90% were purchased from Nanocyl SA (Belgium). Dopamine hydrochloride (DA) and trimethylolaminomethane (Tris) were purchased from Aladdin Reagents. Polyvinyl alcohol (PVA) with brand number 1799 and alcoholysis degree 99% was purchased from Sigma-Aldrich Co., Ltd (China). Hydrochloric acid (HCl, 37%), glutaraldehyde (GA,50% aqueous solution), n-hexane were provided by Chengdu Colon Chemical Co., LTD (China). Commercial cotton cloth is purchased from Hebei Yongsheng Cotton Weaving Factory (China). Polydimethylsiloxane (PDMS, Sylgard 184A) and curing agent (Sylgard 184B) were purchased from Dow Corning. Methylene Blue (MB), Congo Red Congo Red (CR), anhydrous potassium carbonate K_2CO_3,

Methyl Orange (MO) were provided by from Adamas. Anhydrous magnesium sulfate $MgSO_4$, NaCl, $CaCl_2$, $NiSO_4.6H_2O$, $CuSO_4$ and $ZnCl_2$ were purchased from Greagent. Bohai Sea pure natural sea water purchased from Bohai Liaoshen shop. Deionized water was obtained from a water purifier (UL pure KE0119) and used in all experiments.

Method

Preparation of VA-PDA@CNT/PVA aerogel

The specific steps of preparing PDA @ CNT hybrids are as follows. First, 1g of CNT was weighed and added to 500 ml of deionized water to disperse CNT evenly by ultrasound. Then 0.61 g of Tris was added to the above solution by magnetic stirring until dissolved, and the pH of the solution was adjusted to 8.5 and then 1g of DA was added into the solution for 2h. Finally, the PDA/CNT reaction solution was filtered, washed and dried to obtain PDA@CNT hybrids.

The specific steps of preparing VA-PDA@CNT/PVA aerogel are as follows. Firstly, PVA particles were added to deionized water and dissolved at 90 ℃ to prepare 30mg/ml PVA solution. The prepared PDA@CNT hybrid was ultrasonically dispersed in deionized water to prepare 30mg/ml PDA@CNT dispersion solution. Secondly, 10g PVA solution was taken and added to 10g PDA@CNT dispersion solution by drops, stirring (1000rpm) for 3h and ultrasonic for 5min. Then, 1.82g dilute hydrochloric acid and 0.18g glutaraldehyde were added into the mixed dispersing solution and stirred for 20min to prepare precursor solution. The precursor solution was then poured into a mold surrounded by polytetrafluoroethylene and copper at the bottom. The bottom of

the mold was exposed to a liquid nitrogen bath at-110 ℃ until the precursor solution was completely frozen. The obtained gel was freeze-dried at -50 ℃, 1 Pa for 48 h and thermally cross-linked at 80 °C for 2 h to prepare VA-PDA@CNT/PVA aerogel (inner diameter=20mm) with CNT content of 50wt%. The VA-PDA@CNT/PVA aerogels with CNT content of 10wt %, 30wt % and 70wt % were also prepared by the same method. For comparison, for R-PDA@CNT/PVA aerogels with random structure, the same amount of precursor solution was poured into a hollow copper column and placed in a refrigerator at -20 ℃ to prepare gel, and then freeze-dried at-50 ℃, 1 Pa for 48 h. At this time, the temperature has no direction and the aerogel with disordered structure can be formed.

Preparation of Cotton/CNT/PDMS (CCP) film

First, 5g CNT and 0.5g SDBS were added to 500ml deionized water and treated with strong ultrasound for 5h to form a stable CNT suspension. Then, the neat cotton with a diameter of 80mm and a diameter of 20mm is cut in the center is immersed in the CNT/H_2O dispersion solution., and the CNT was coated on the neat cotton cloth by ultrasonic deposition method. Then the cotton cloth was dried at 90 ℃ to obtain Cotton/CNT film. And the Cotton/CNT film was immersed in PDMS/curing agent (10/1, wt/wt) n-hexane solution. Finally, it was taken out and dried at 80 ℃ for 5 h to obtain a hydrophobic photothermal CCP film.

Preparation of simulated heavy metal wastewater

1.5g $MgSO_4$, 1.5g $CuSO_4$, 1.5g $ZnCl_2$ and 1.5g $NiSO_4$ were added into 1L of water, and then mixed and stirred until completely dissolved to prepare simulated heavy

metal wastewater.

Preparation of dye wastewater

50 mg CR was added into 1 L water, and then mixed and stirred until completely dissolved to prepare CR contaminated wastewater. For the same concentration of MO and MB dye wastewater, the same method is also used to prepare.

Characterization

The morphology of CNT was observed by transmission electron microscope (TEM, JEM100CX II, Japan). The composition and structure of CNT and PVA aerogel samples were analyzed by Fourier transform infrared (FT-IR). The compositions of CNT and Cotton samples were analyzed by X-ray photoelectron spectroscopy (XPS, XSAM800). Non-isothermal thermogravimetric analyzer (TGA, Q500, USA) was used to analyze the composition of CNT samples. The morphology and microstructure of CCP film and PVA aerogel were observed by scanning electron microscope (SEM, Navo Nano SEM 450), and the microstructure of CNT, PVA aerogel and CCP film was analyzed by energy dispersive spectrometer (EDS). The porosity and specific surface area of PVA aerogel were analyzed by automatic physical adsorption instrument (BET, ASAP 2460, USA). The surface properties of CCP film were analyzed by X-ray diffractometer (XPS, XSAM800, UK). The water contact angle of CCP film and PVA aerogel was measured at room temperature using contact angle tester (Kruss DSA100, Germany). UV-Vis-NIR spectrophotometer (UV3600, Japan) was used to evaluate the absorption capacity of CCP film and PVA aerogel to sunlight. The ion concentration before and after seawater desalination by solar water evaporation system was measured using the inductively coupled plasma mass spectrometry (ICP-MS; agilent 7700x). The

concentration of dye before and after purification by solar water evaporation system was measured by ultraviolet-visible spectrophotometer (VARIAN Cary 50). The thermal diffusion coefficient α of CCP film and PVA aerogel was measured by laser scatter (LFA 467 Hyper Flash Netzsch, Germany), and then the equation $k = \alpha \times \rho \times c_p$ (α: thermal diffusion coefficient, ρ: density, c_p: special heat capacity) was used to calculate the thermal conductivity, where ρ was measured by Archimedes method (JA203 Puchun Instruments, China), and c_p was measured by DSC sapphire method. The Zeta potential of CNT and PDA@CNT was measured using a Zeta potentiometer. The compression properties of PVA aerogel were measured by a universal mechanical machine (Instron 5967, USA).

Solar evaporation experiment

A series of comparative experiments of R-PDA@CNT/PVA (with and without CCP film) and VA-PDA@CNT/PVA (with and without CCP film) evaporators were carried out under the convective conditions of 20 ℃, 40 % humidity and 0 ms^{-1} convective velocity to systematically study the evaporation performance of evaporators. For the evaporation of PDA@CNT/PVA evaporators without CCP film, each sample was continuously irradiated for 1h under 1sun irradiation, and the mass change of water during evaporation was simultaneously recorded by a high-precision (0.1mg) analytical balance. To avoid the influence of the direct evaporation of the bottom bulk water on the test results, a circular hole with a diameter of 20 mm was carved in the center of the EPS foam and the aerogel was placed into it.Then, put them into a petri dish filled with water for water evaporation experiment. The heights of the aerogel immersed in water and exposed to the outside were 15 mm and 25 mm,

respectively. In addition, during the evaporation process, the infrared thermal imager (FLIR-T600) was used to record the temperature of five different points on the surface and side of the evaporator and take the average to obtain the temperature of the surface and side of the evaporator. For the evaporation of PDA@CNT/PVA with CCP film evaporators, CCP film was placed flat on EPS foam and tested under the same conditions for 1h or 10h (salt-tolerant) using the same method. The open-circuit voltage and short-circuit current of the solar evaporator were measured by a digital multimeter (Owon B35T +).

COMSOL simulation

COMSOL simulation of heat transfer in R-PDA@CNT/PVA (with and without CCP film) and VA-PDA@CNT/PVA (with and without CCP film).The heat transfer equation of porous media is as follows:

$$-\nabla \cdot \left(k\nabla T + L_v \delta_p \nabla\left(\phi p_{\text{sat}}\right)\right) = 0 \tag{1}$$

where T represents the temperature, k represents the thermal conductivity, L_v represents the latent heat, δ_p represents air vapor permeability, ϕ represents relative humidity, p_{sat} represents aturated pressure.

The conducted heat flux q_{cond} is as follows:

$$q_{cond} = k\nabla T \tag{2}$$

Radiant heat flux q_{rad} is as follows:

$$q_{rad} = \varepsilon\sigma A\left(T^4 - T_{ext}^{\ 4}\right) \tag{3}$$

where T_{ext} represents ambient temperature, ε represents emissivity, σ represents stefan-Boltzmann constant, and A represents the area.

Air convective heat flux q_{coev} is as follows:

$$q_{coev} = h(T_{ext} - T) \quad (4)$$

h represents convective heat transfer coefficient:

$$h = \frac{k}{L} 0.27 Ra_L^{1/4} \quad (5)$$

where L represents the characteristic length and is the area/perimeter. Ra represents Rayleigh number:

$$Ra = \frac{\rho^2 g \beta C_p |T_{ext} - T| L^3}{k\mu} \quad (6)$$

where ρ represents density, g represents gravitational constant, C_p represents specific heat capacity, β represents coefficient of thermal expansion, μ represents dynamic viscosity.

Calculation. S1 the water content and water transport rate of R-PDA@CNT/PVA evaporator and VA-PDA@CNT/PVA aerogel

The water content of aerogel samples is calculated as follows[17]:

$$Q = \frac{W}{W_{dry}}$$

Where Q is the water content, W is the mass of water in the swelling aerogel sample, and W_{dry} is the mass of the corresponding dry aerogel sample.

The aerogel water transport rate is calculated as follows:

$$V = \frac{0.5Qs}{t}$$

Where V is the water transport rate, $0.5Q_s$ is the water content of the aerogel sample at half saturation, and t is the time required for the aerogel sample from half saturation to

saturation.

Calculation. S2 the equivalent evaporation enthalpy of VA-PDA@CNT/PVA evaporator and R-PDA@CNT/PVA evaporator from dark evaporation.

Bare liquid water, R-PDA@CNT and VA-PDA@CNT evaporators with the same equivalent surface areas were simultaneously placed in a sealed container of supersaturated potassium solution for the dark evaporation experiment. The evaporation rates of bare liquid water, R-PDA@CNT and VA-PDA@CNT evaporator samples were recorded, and the equivalent evaporation enthalpy (E_{equ}) of water in the evaporator was calculated using the following formula:

$$m_g E_{equ} = m_0 E_0$$

Where m_g is evaporator's mass change, E_{equ} is equivalent evaporation enthalpy of water in the evaporator, m_0 is bare liquid water's mass change, E_0 is water evaporation enthalpy (2450 J g^{-1}).

Calculation. S3 the evaporation efficiency of evaporator

The evaporation efficiency (η) of evaporator is calculated by:

$$\eta = mE_{equ}/C_{opt}P_0$$

Where m is the evaporation rate (the corresponding dark evaporation rate was subtracted), Eequ is the evaporation enthalpy of water, P_0 is irradiation power, C_{opt} is optical concentration captured by the absorber surface.

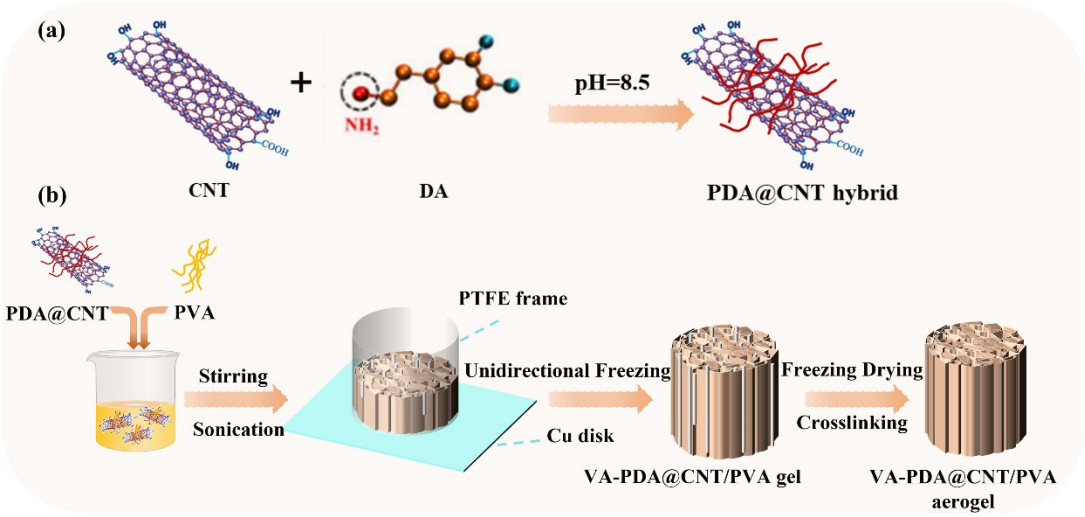

Figure S1 Scheme of preparation process of PDA@CNT hybrid (a) and VA-PDA@CNT/PVA aerogel (b)

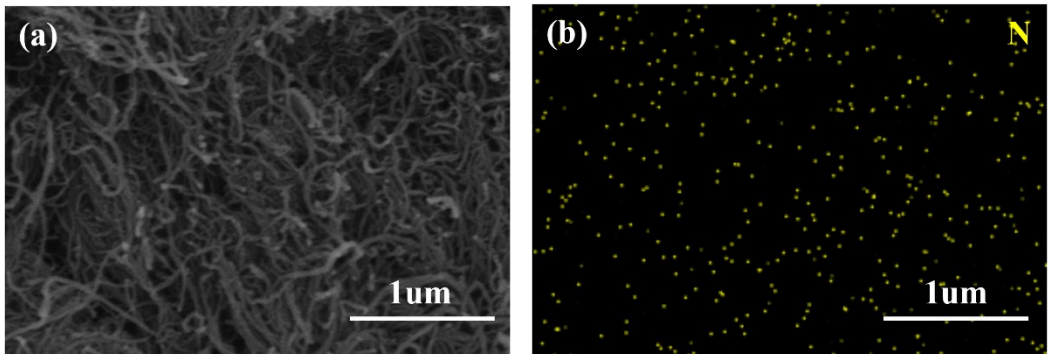

Figure S2 SEM images (a) and EDS mapping (b) of PDA@CNT

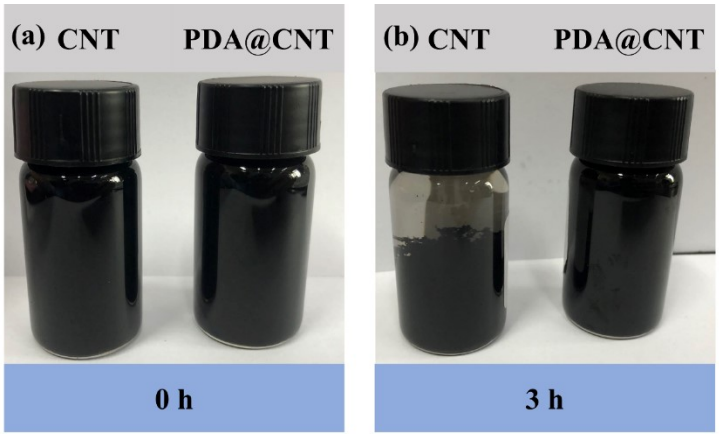

Figure S3 Digital images of dispersion of CNT and PDA@CNT aqueous suspensions (0.2 mg/ml) after settling times of 0h (a), 3h (b).

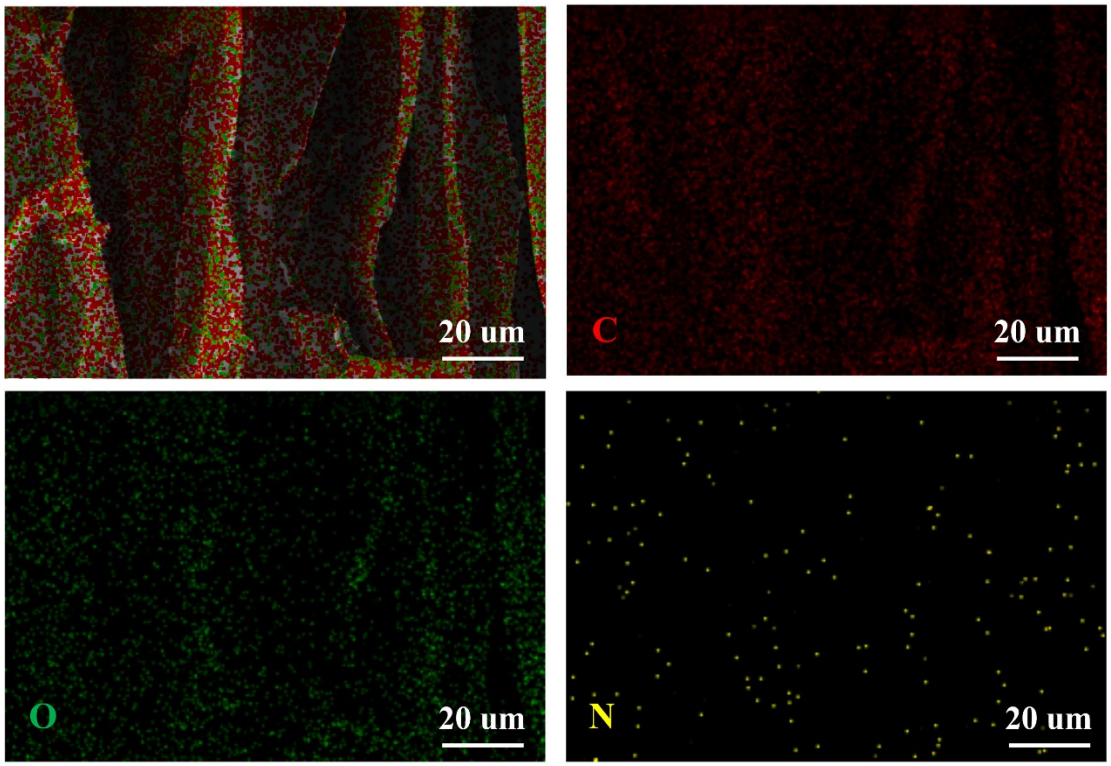

Figure S4 EDS element mapping of the longitudinal section surface of VA-PDA@CNT/PVA aerogel

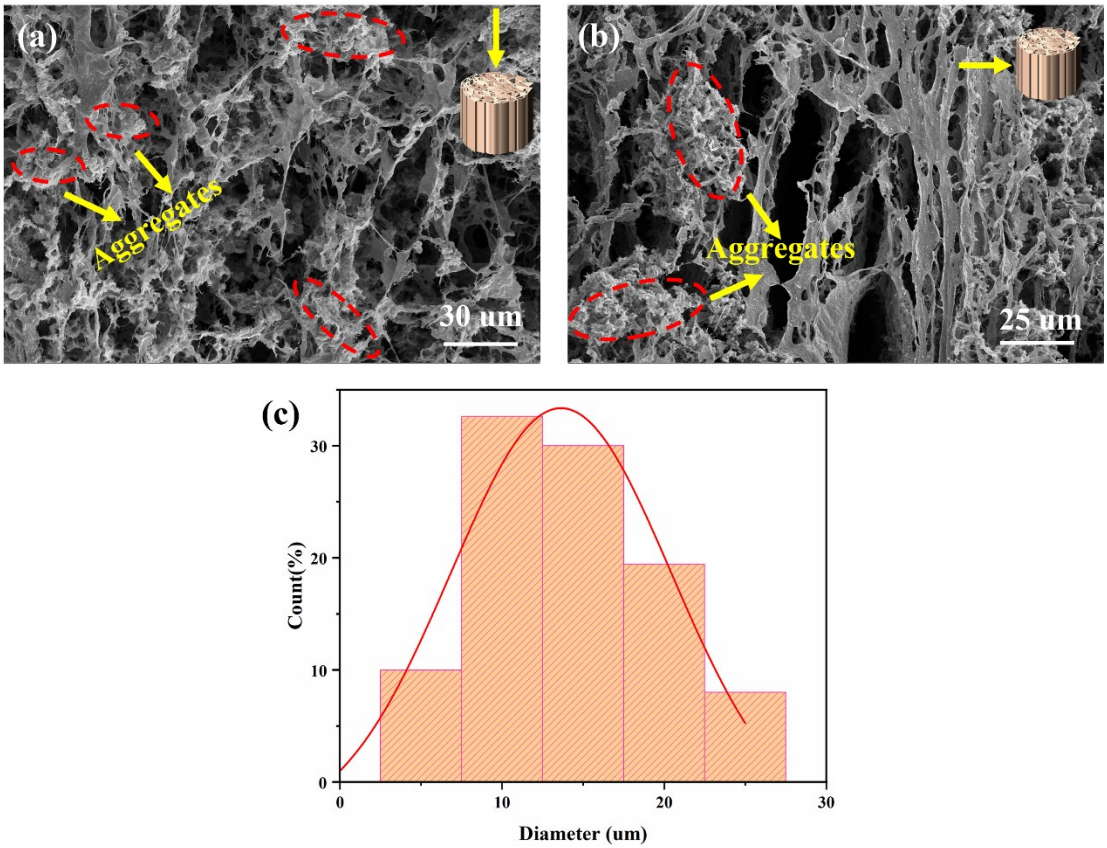

Figure S5 SEM images of the transverse section (a) and longitudinal section (b) of the VA-CNT/PVA (-110℃) aerogel and the corresponding diameter distributions of the micro-pores of

the aerogel (c)

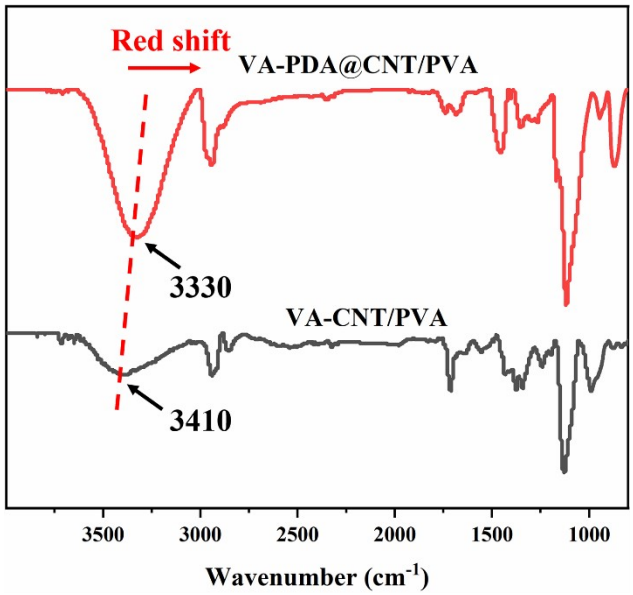

Figure S6 FTIR spectra of the VA-PDA@CNT/PVA and VA-CNT/PVA aerogel

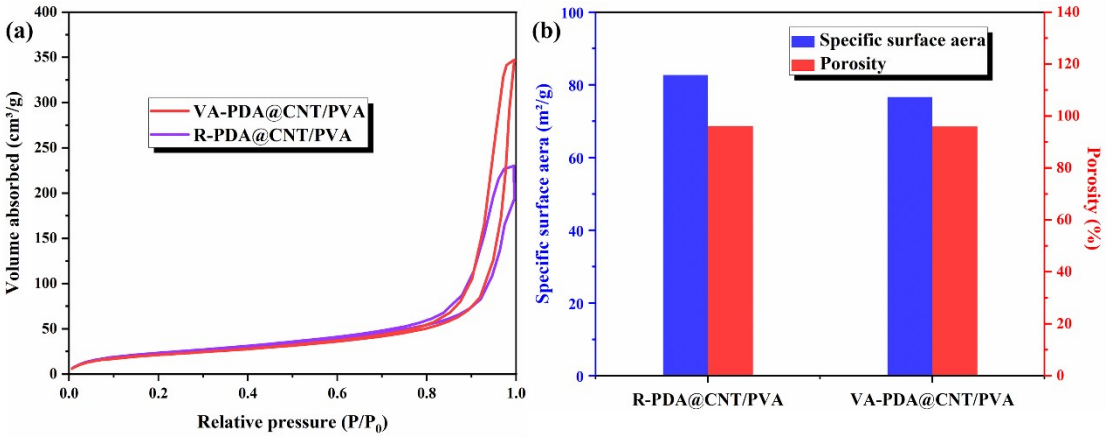

Figure S7 (a) nitrogen adsorption–desorption isotherms of VA-PDA@CNT/PVA snd R-PDA@CNT/PVA aerogel, (b) specific surface area and porosity of VA-PDA@CNT/PVA snd R-PDA@CNT/PVA aerogel.

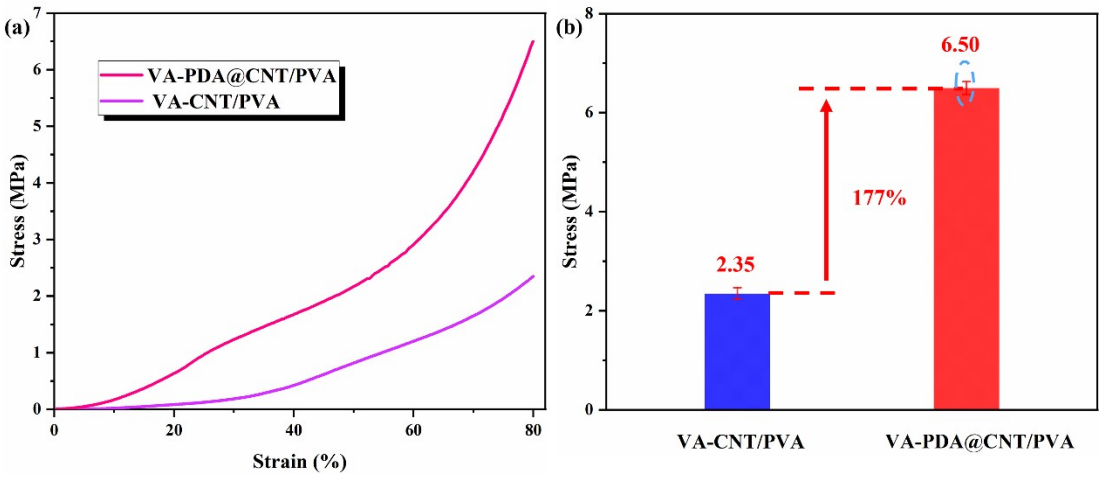

Figure S8 Compressive stress-strain curves of VA-PDA@CNT/PVA and VA-CNT/PVA aerogel, (b) the comparison of compressive stress of VA-PDA@CNT/PVA and VA-CNT/PVA aerogel at 80% strain.

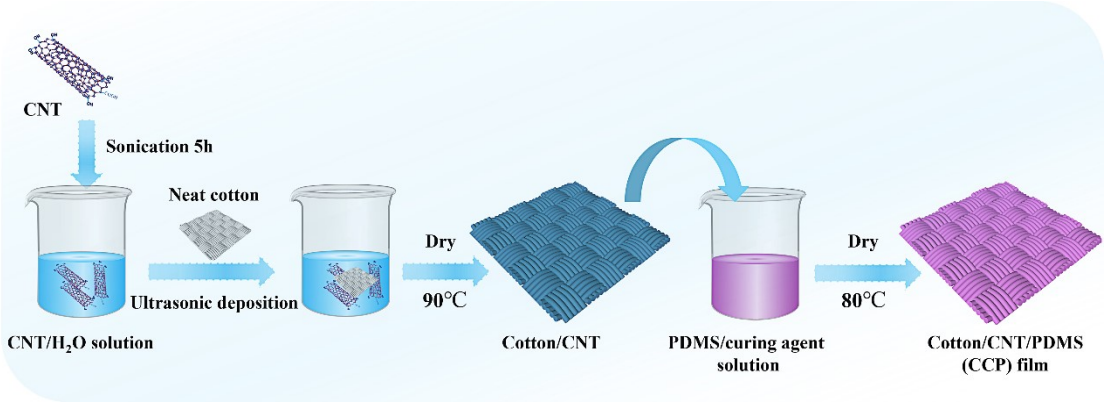

Figure S9 Scheme of preparation process of CCP film

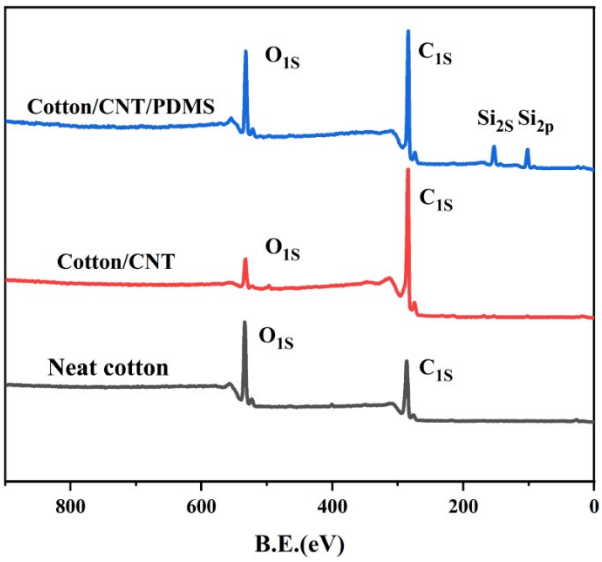

Figure S10 XPS full spectrum of neat cotton, cotton/CNT, cotton/CNT/PDMS

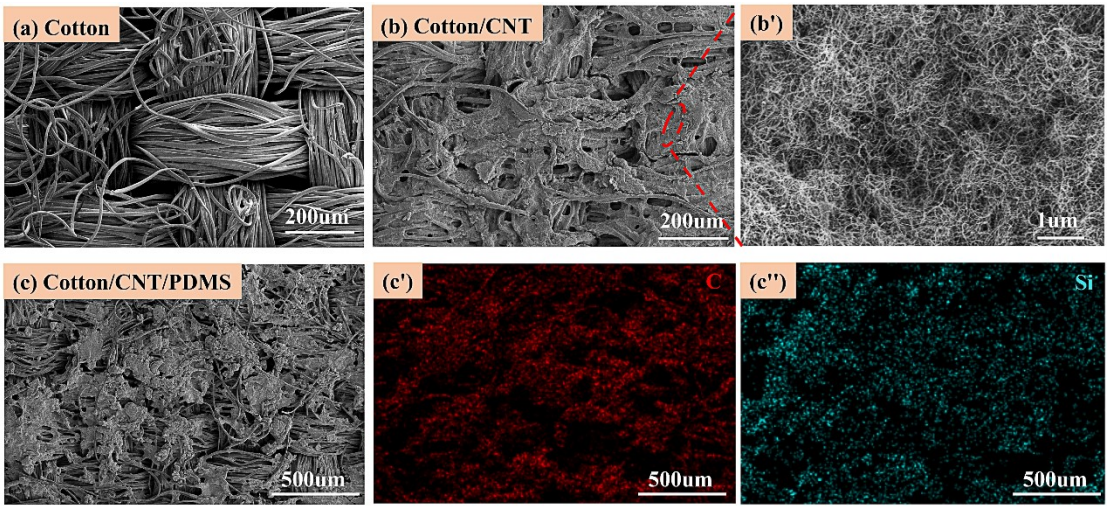

Figure S11 SEM images of neat cotton (a), cotton/CNT (b-b′), Cotton/CNT/PDMS (c) and (c-c′) EDS element mapping of (c).

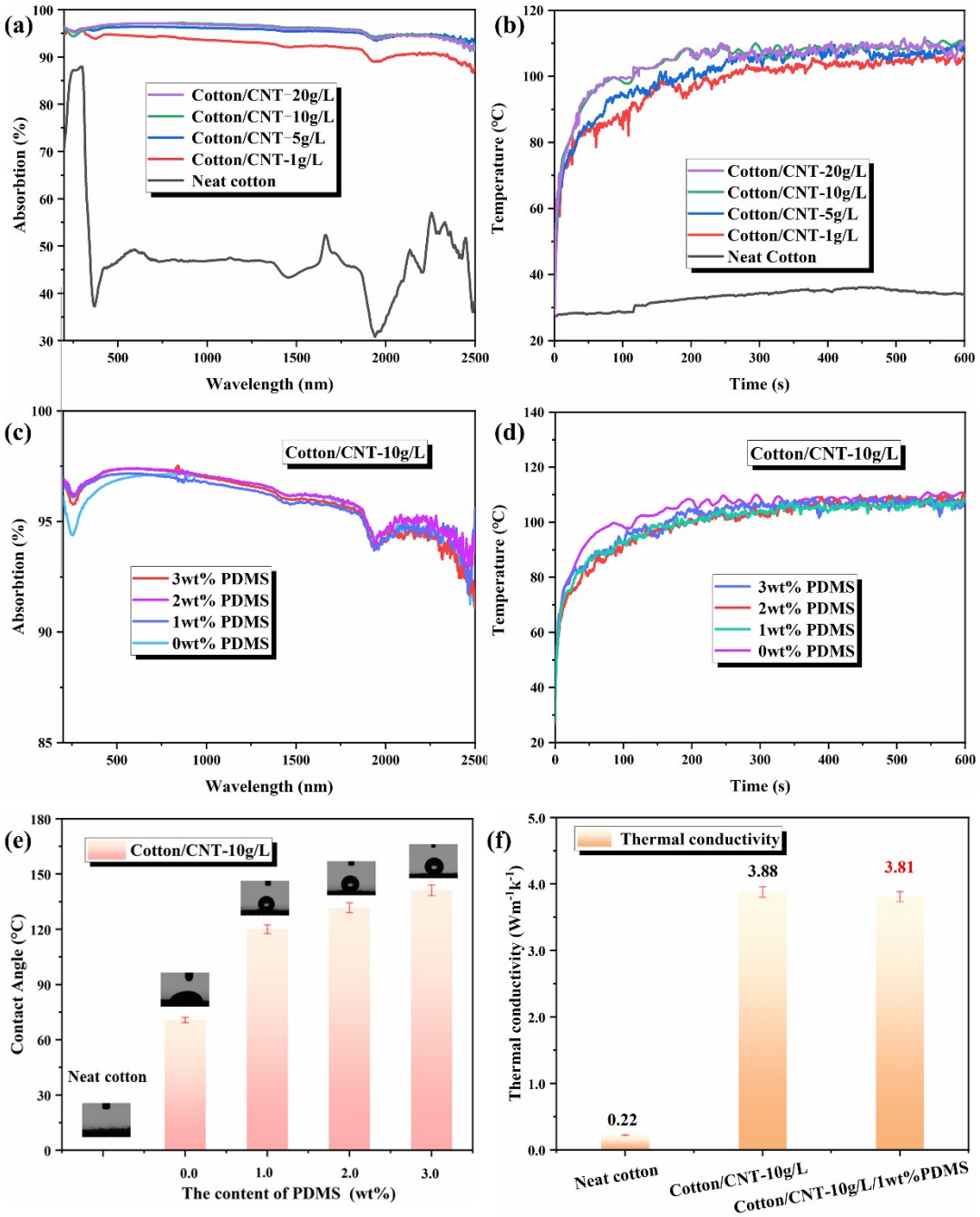

Figure S12 (a) The UV-vis-NIR spectra and (b) surface temperatures evolution profiles of neat cotton, cotton/CNT at different concentration of CNT, (c) UV-vis-NIR spectra and (d) surface temperatures evolution profiles of cotton/CNT-10g/L at different concentration of PDMS, (e) water contact angle of neat cotton and cotton/CNT-10g/L at different concentration of PDMS. (f) Thermal conductivity of neat cotton, cotton/CNT-10g/L, cotton/CNT-10g/L-1wt%PDMS.

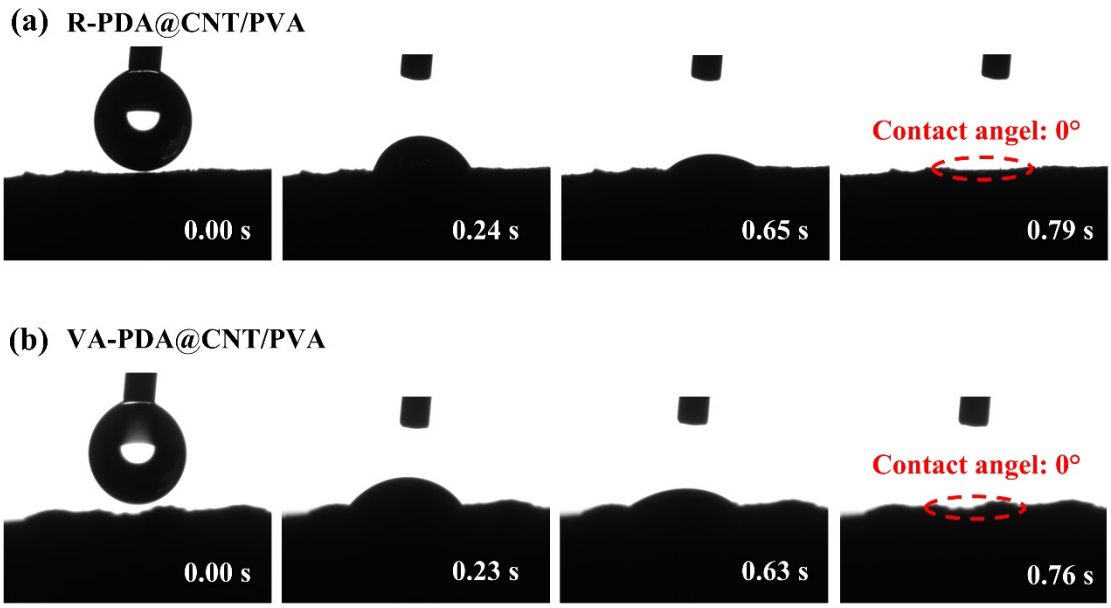

Figure S13 Water contact tests of (a) R-PDA@CNT/PVA, (b) VA-PDA@CNT/PVA aerogels

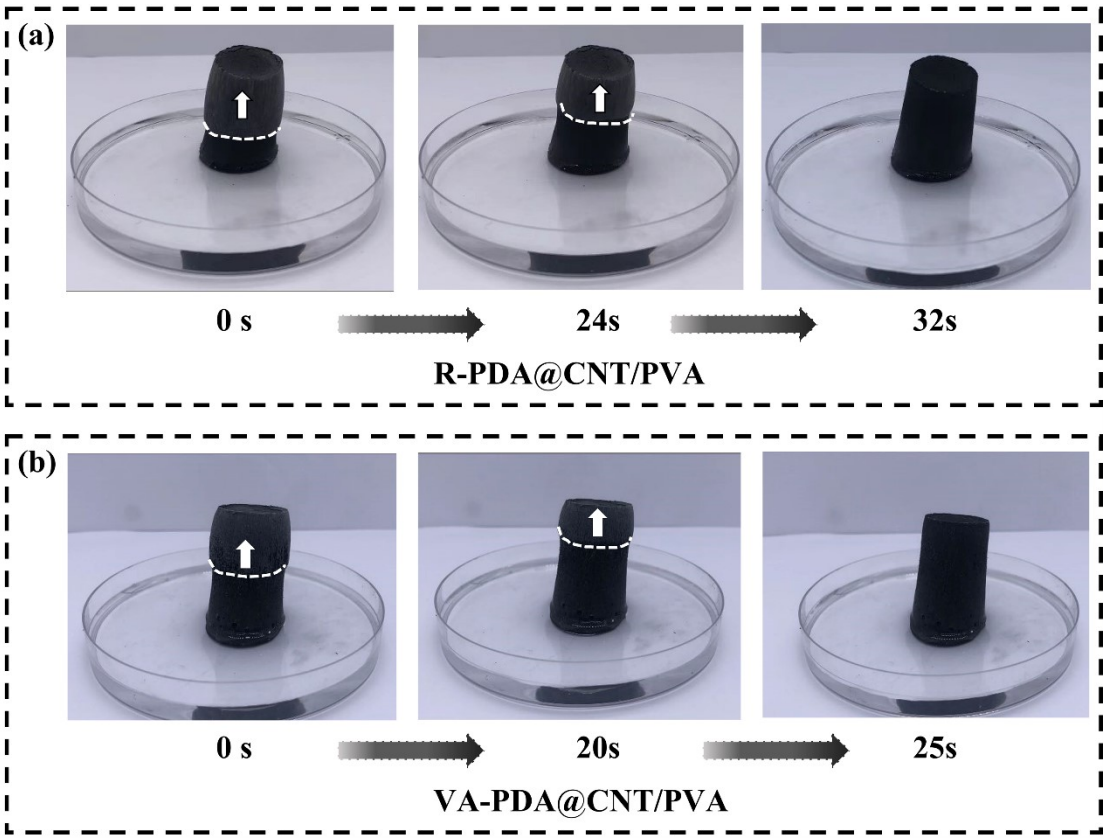

Figure S14 The water transport status of (a) R-PDA@CNT/PVA, (b) VA-PDA@ CNT/PVA aerogels over time

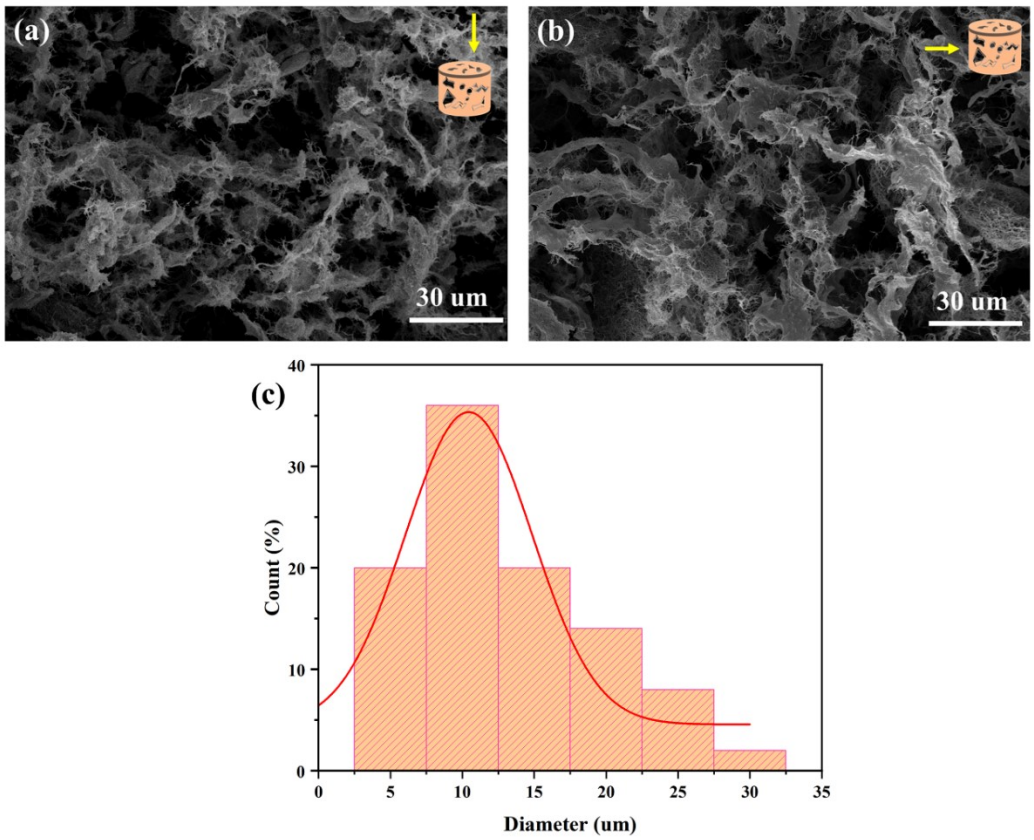

Figure S15 SEM images of the transverse section (a) and longitudinal section (b) of the R-PDA@CNT/PVA (-110℃) aerogel and the corresponding diameter distributions of the micro-pores of the aerogel (c)

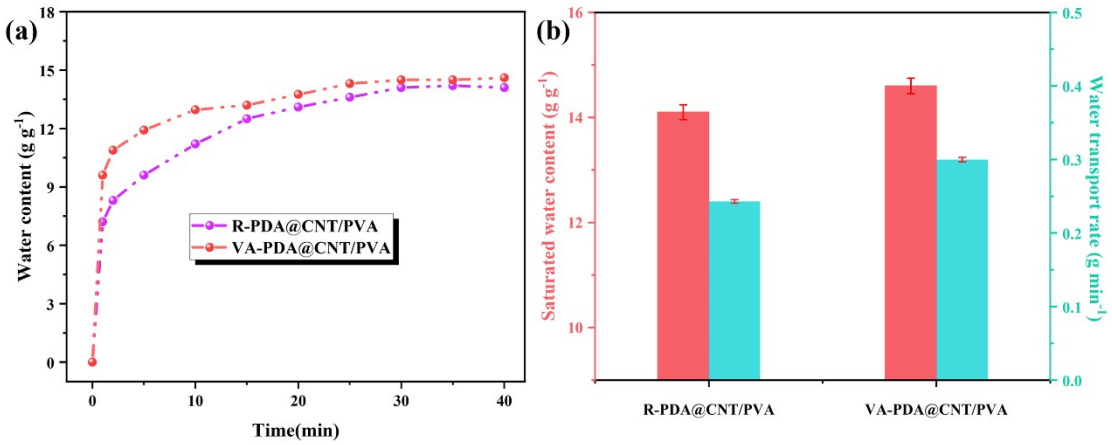

Figure S16 (a) Water content curves of R-PDA@CNT/PVA and VA-PDA@CNT/PVA aerogel with time, (b) the saturated water content and water transport rate of R-PDA@CNT/PVA and VA-PDA@CNT/PVA aerogel

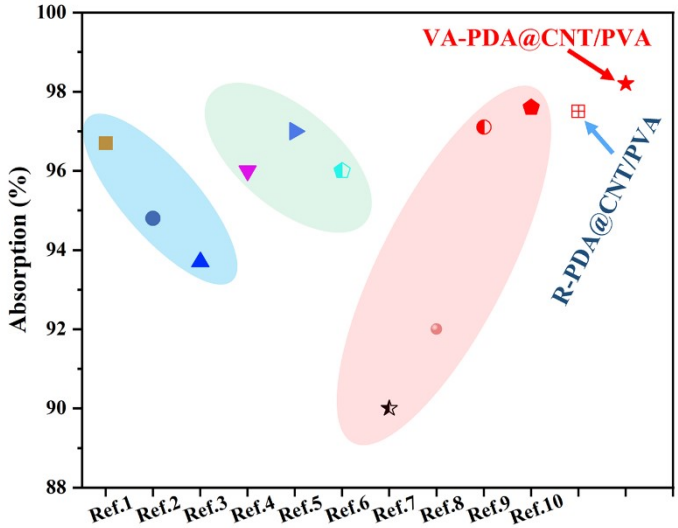

Figure S17 comparison of light absorbance of the VA-PDA@CNT/PVA aerogel evaporator and reported evaporators[1-10]

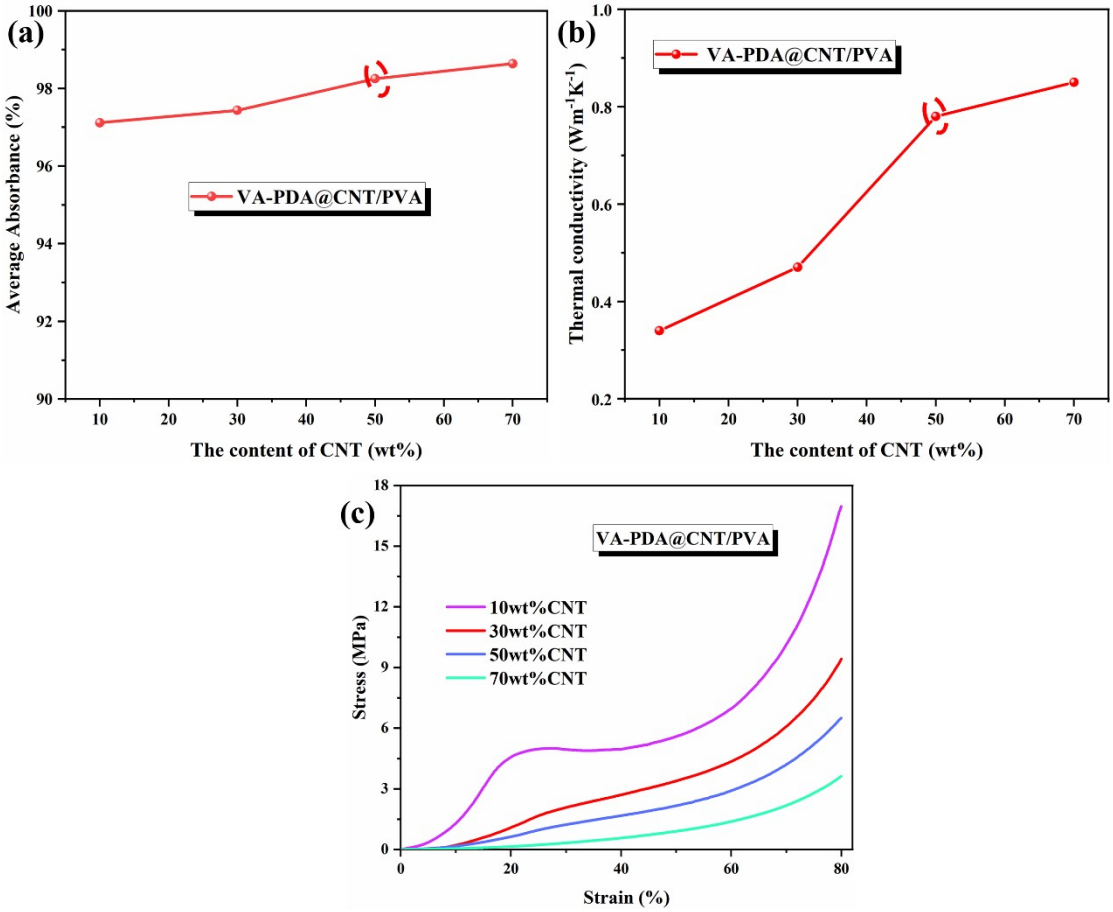

Figure S18 (a) Average absorbance of VA-PDA@CNT/PVA aerogel with different CNT content in the range of the entire solar spectrum (200-2500 nm), (b) thermal conductivities of VA-PDA@CNT/PVA aerogel with different CNT content, (c) Compressive stress-strain curves of VA-PDA@CNT/PVA aerogel with different CNT content.

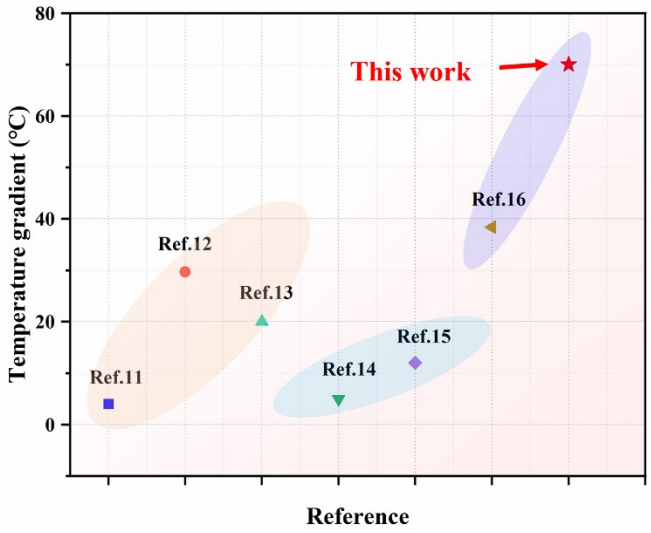

Figure S19 Comparison of the temperature gradient between PDA@CNT/PVA aerogel evaporator and CCP film with those those reported in literature[11-16]

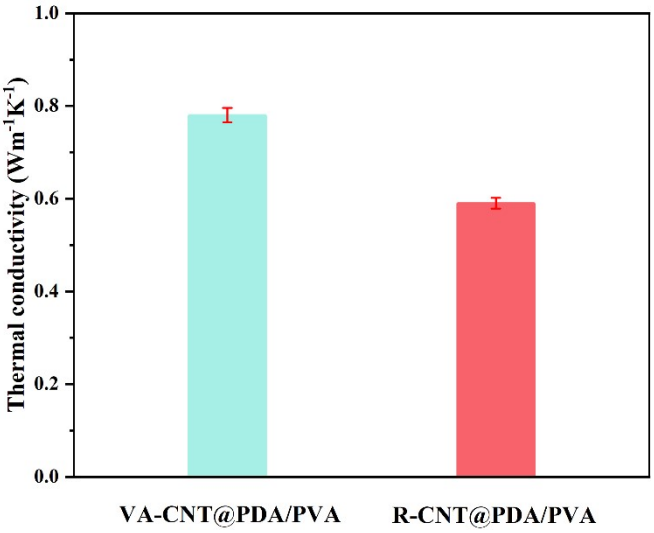

Figure S20 the comparison of thermal conductivity of VA-PDA@CNT/PVA aerogel and R-PDA@CNT/PVA aerogel in wet condition.

Table S1 Water evaporation enthalpy and evaporation rate of VA-PDA@CNT/PVA with CCP film evaporator under 1sun irradiation are compared with some evaporator reported in the literature

Evaporator	Enthalpy(J g^{-1})	Evaporation rate	Reference
PVA/rGO hydrogel	1400	2.5	17
Plasmon based double-layer hydrogel	1591.12	2.1	18
CNT/bacterial cellulose/wood composite	997	2.9	19
Sea urchin-like carbon coated wood	1810	2.07	20
Porous carbon-coated wood	1427	2.38	21
PPy-coated bacterial cellulose hydrogel	1970	1.78	22
N, O dual-doped carbon foam	1524	2.4	23
Carbon dot-modified starch aeroge	1535	2.29	24
Lignocellulose-based double-layered hydrogel	1667	1.84	25
PDA/ZIF-8/PDA porous wood composite	1146	2.70	26
PDMX/HPP aerogel	1425.61	2.62	27
Ti_2O_3/PVA	930	3.6	28
VA-PDA@CNT/PVA with CCP film	**900**	**6.96**	**This work**

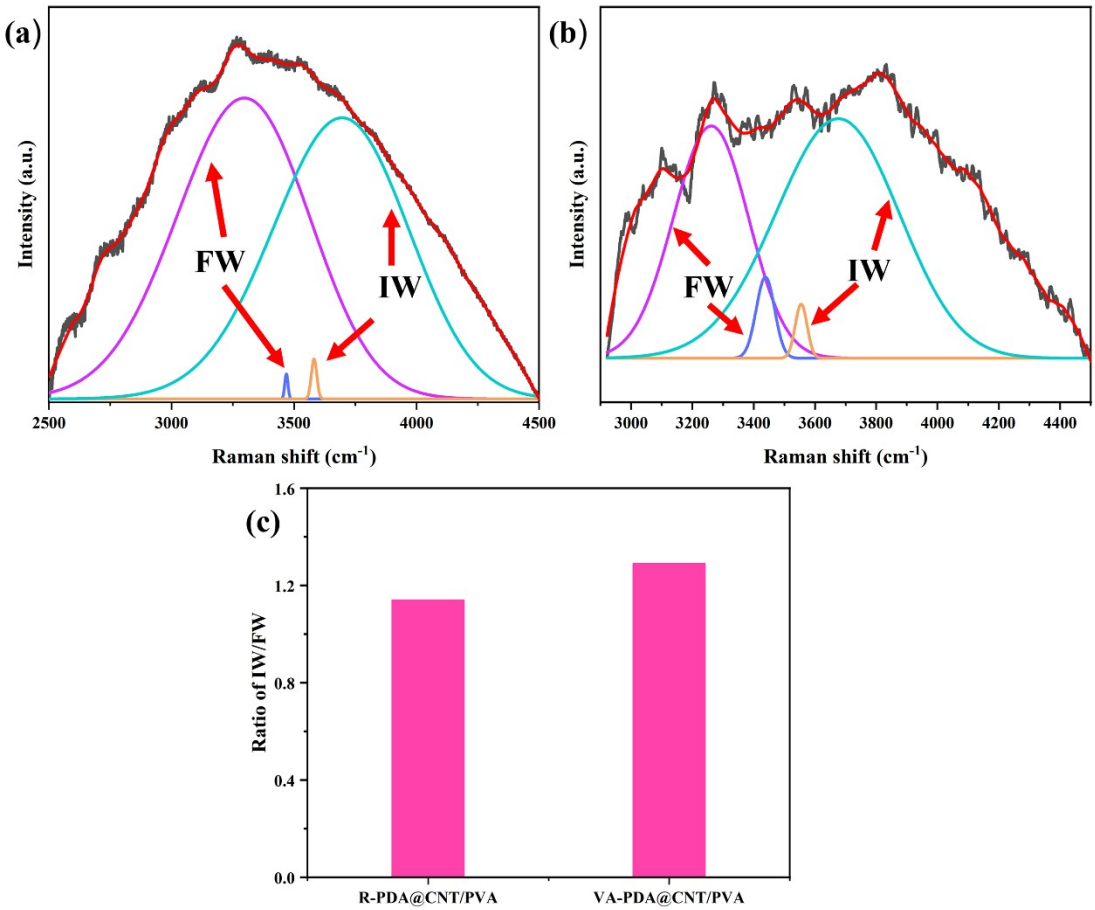

Figure S21 Raman spectrum of water absorbed in the R-PDA@CNT/PVA aerogel(a) ,VA-PDA@CNT/PVA aerogel and (c) the ratio of IW to FW of R-PDA@CNT/PVA and VA-PDA@CNT/PVA

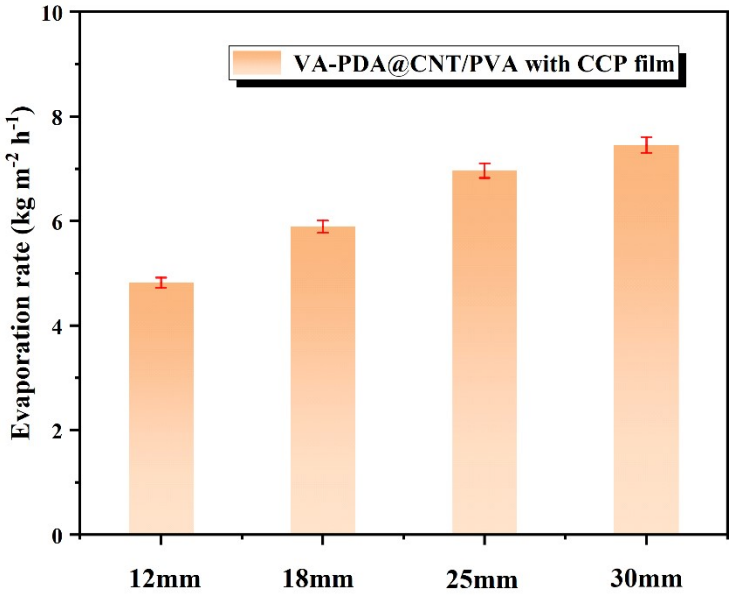

Figure S22 Average evaporation rates of the VA-PDA@CNT/PVA with CCP film with different evaporation heights recorded under one-sun illumination

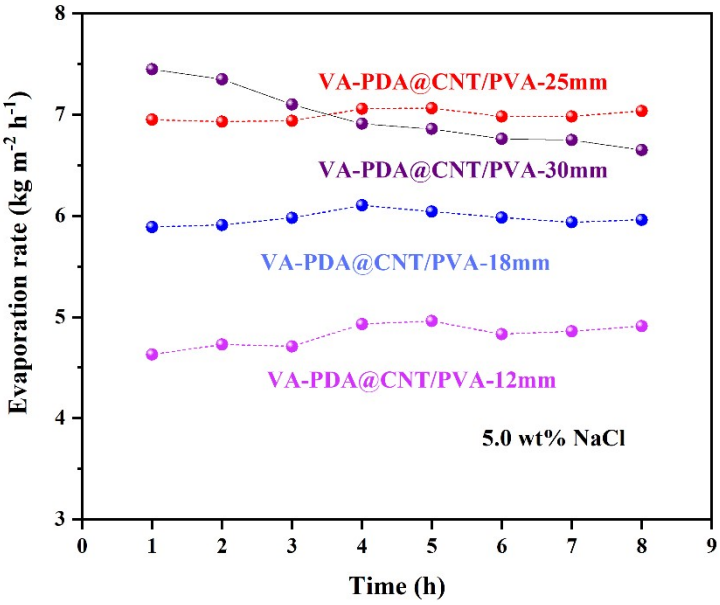

Figure S23 The evaporation rates of VA-PDA@CNT/PVA with CCP film with different evaporation heights under 1sun irradiation in 5.0 wt% Nacl for 8h

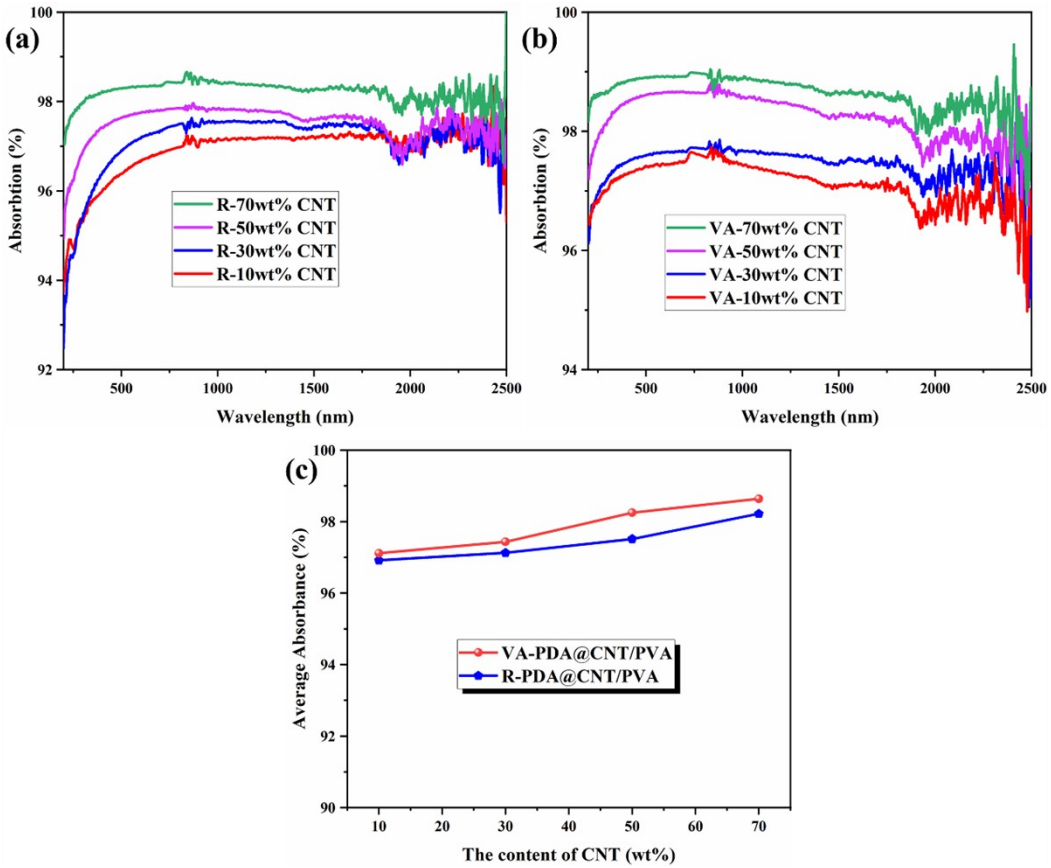

Figure S24 UV-vis-NIR absorption spectra of R-PDA@CNT/PVA (a), VA-PDA@CNT/PVA aerogel (b) with different CNT content, (c) the comparison of average absorbance of R-PDA@CNT/PVA and VA-PDA@CNT/PVA aerogel with different CNT content.

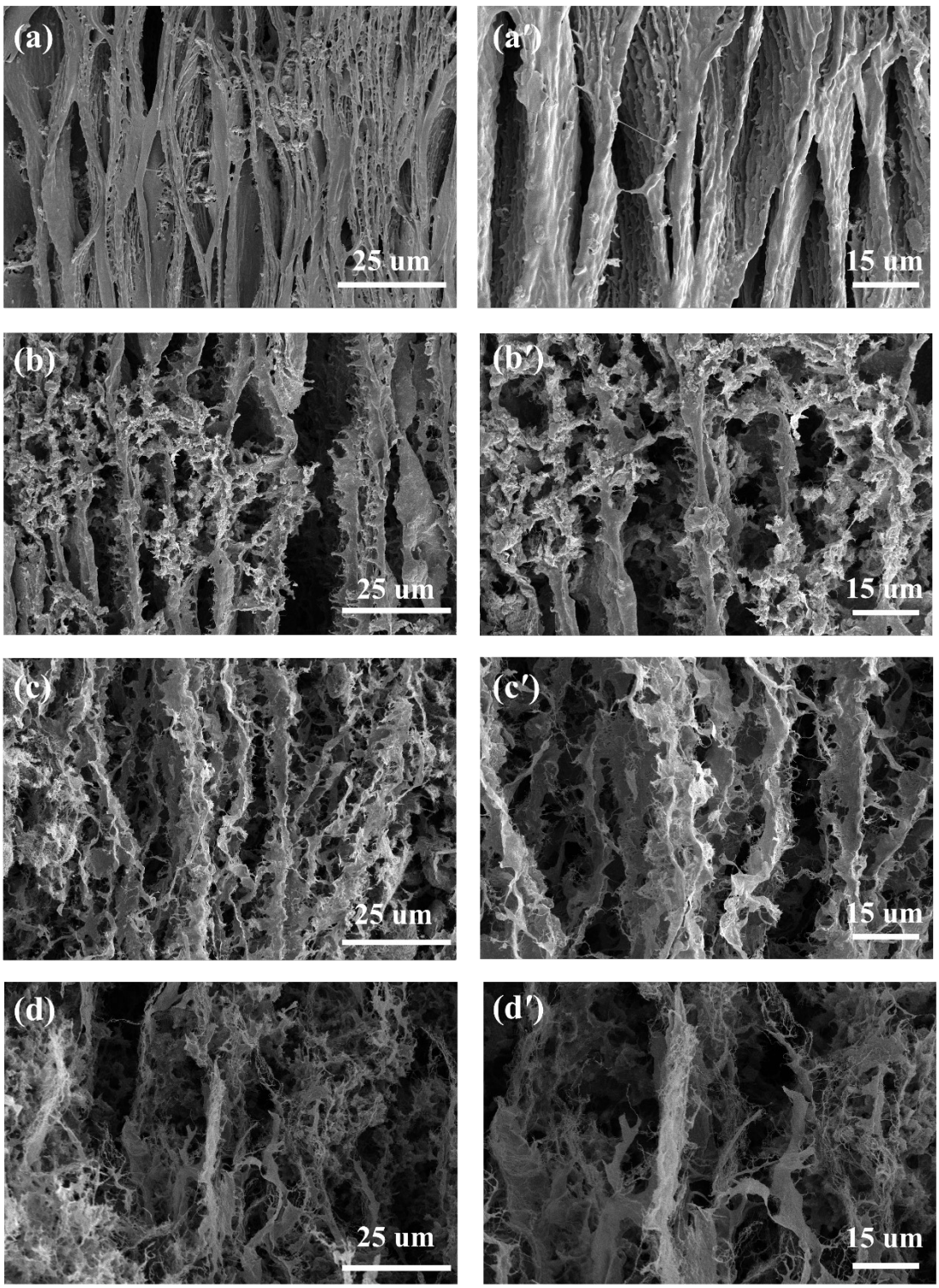

Figure S25 SEM micrographs of the vertical aligned surface of the VA-PDA@CNT/PVA aerogels with different CNT weight percentages: (a, a′) 10wt%; (b, b′) 30 wt%;(c,c′) 50 wt%; (d,d′) 70 wt%

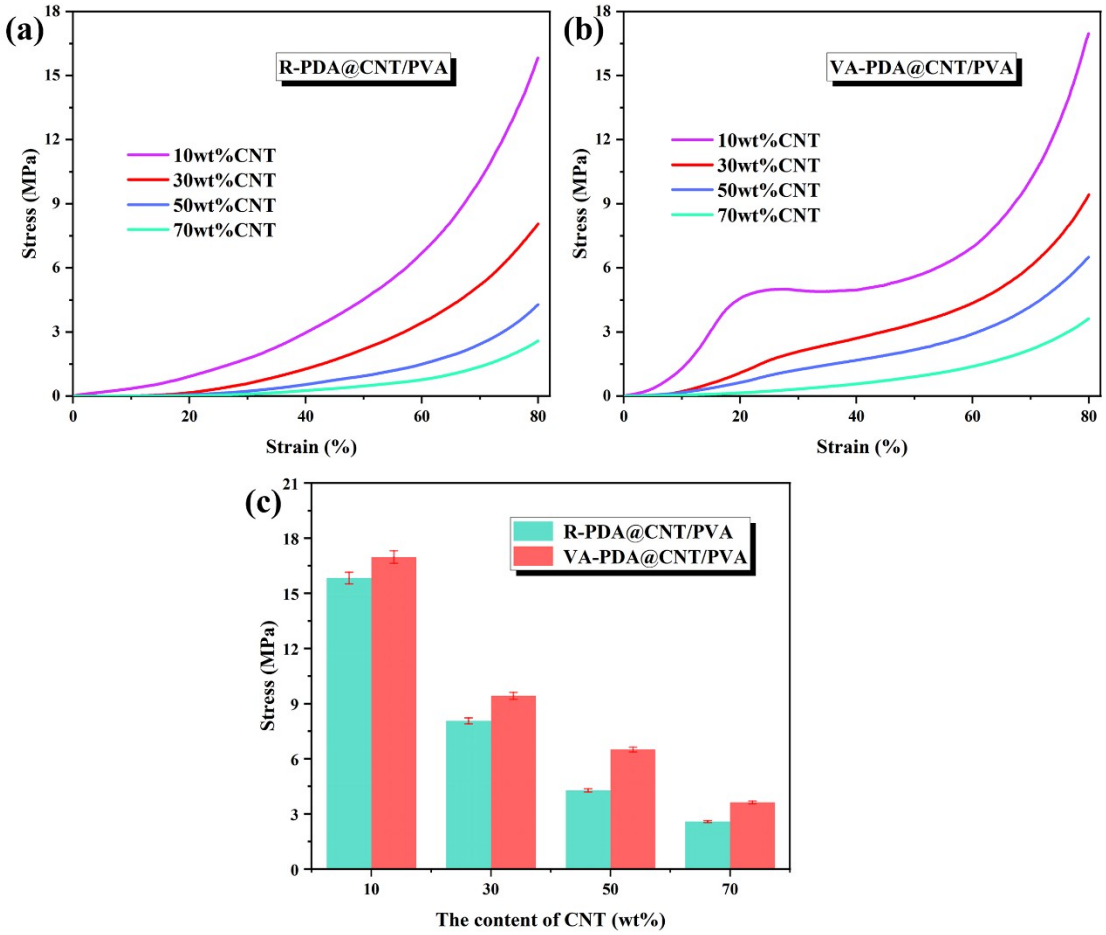

Figure S26 (a,b) compressive stress-strain curves of VA-PDA@CNT/PVA and R-PDA@CNT/PVA aerogel different CNT content, (c) the comparison of compressive stress of VA-PDA@CNT/PVA and R-PDA@CNT/PVA aerogel at 80% strain.

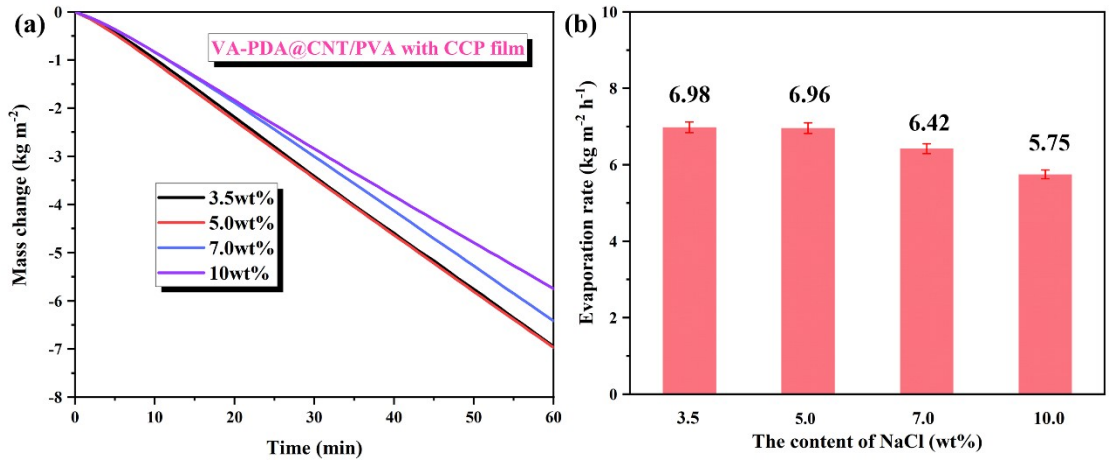

Figure S27 the mass change of VA-PDA@CNT/PVA with CCP film evaporator in different NaCl brine under 1un irradiation, (b) comparison of the evaporation performance of VA-PDA@CNT/PVA with CCP film evaporator in different NaCl brine

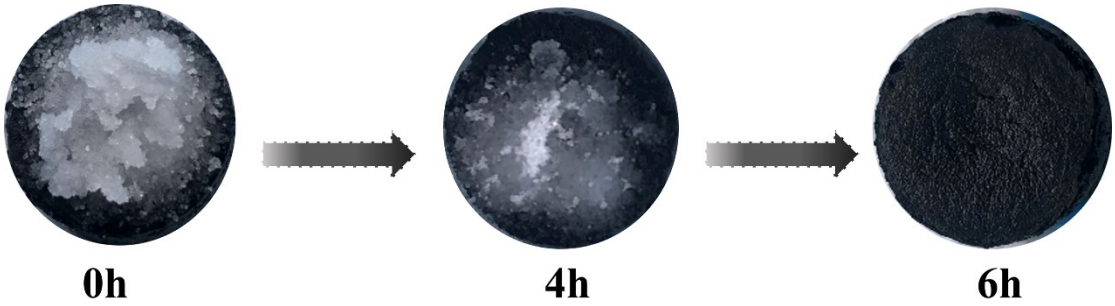

Figure S28 self-cleaning behavior of VA-PDA@CNT/PVA aerogel evaporator

Table S2 Comparison of related parameters of solar-driven desalination

Evaporators	Evaporation rate (kg $m^{-2}h^{-1}$, one sun)	Salinity (wt%)	Continuous operation time (h)	Ref
VA-PDA@CNT/PVA with CCP film	**6.96**	**5**	**10**	**This work**
Surface-carbonized bimodal porous wood membrane	0.8	15	7	9
	0.82	1.1	100	
Acrylic ester resin/carbon nanofibers	1.6	20	5	29
2.5D Cu/CuO foam	4.05	3.5	4	30
	3.4	15	1	
Pd nanoparticles-decorated plasmonic wood	11.8 (10 Sun)	3.5	8	31
Hierarchical graphene foam	6.87(5 Sun)	2.75	7.5	32

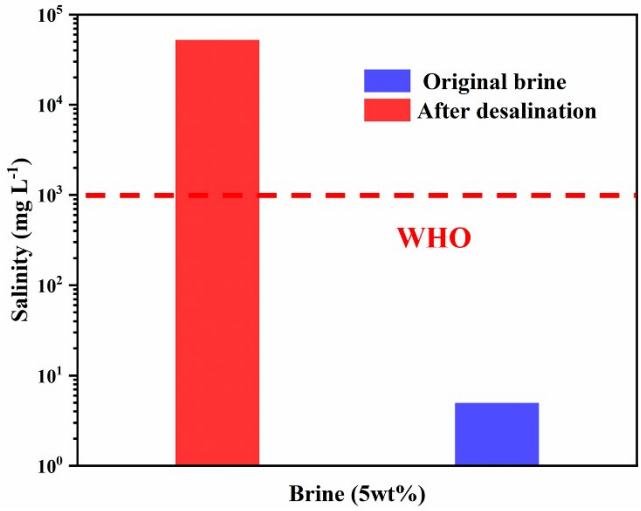

Figure S29 The salinity change of 5.0 wt% NaCl brine before and after desalination treated by VA-PDA@CNT/PVA with CCP film evaporator

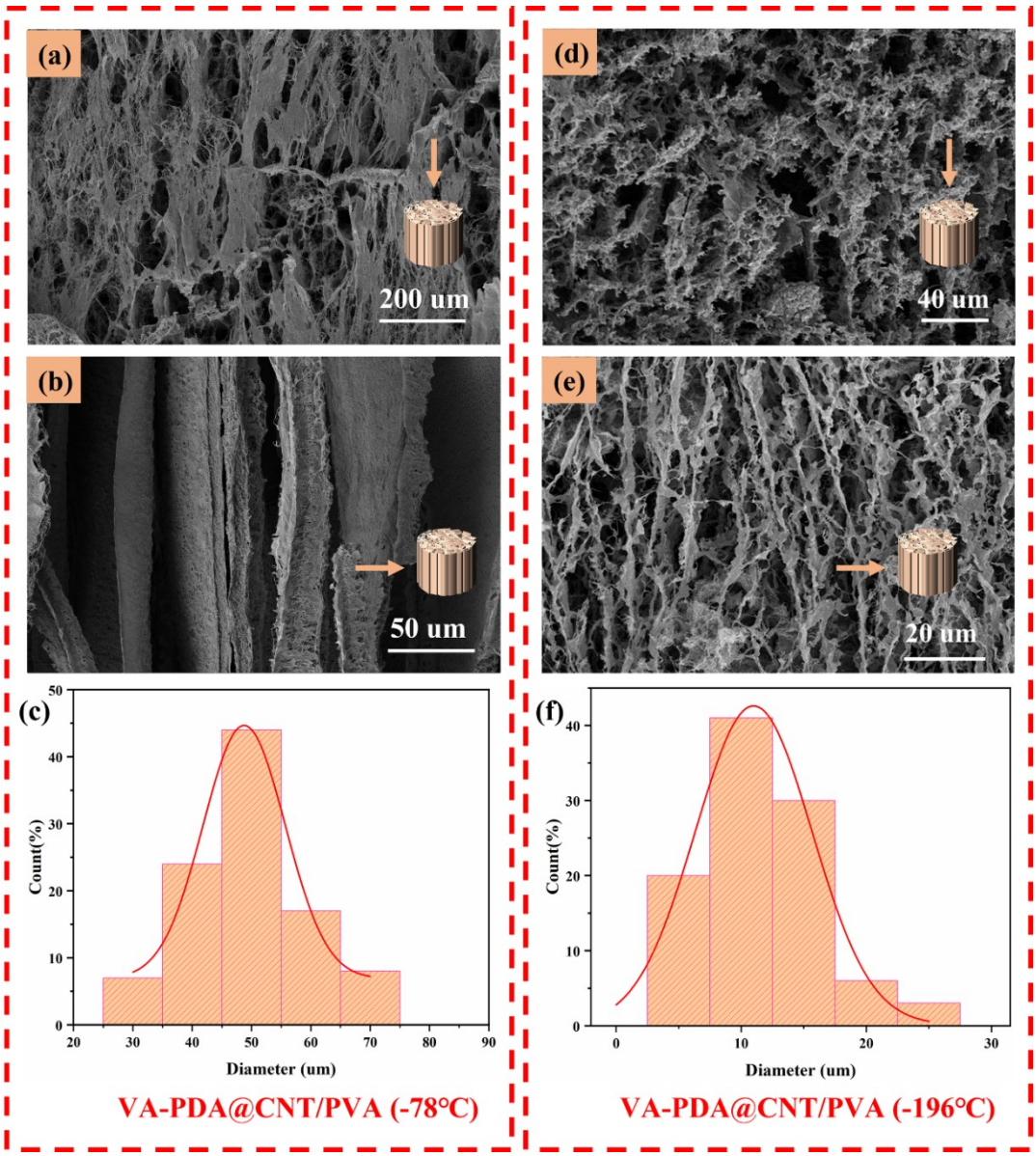

Figure S30 SEM images of the transverse section (a) and longitudinal section (b) of the VA-PDA@CNT/PVA (-78°C) aerogel and the corresponding diameter distributions of the micro-pores of the aerogel (c), SEM images of the transverse section (d) and longitudinal section (e) of the VA-PDA@CNT/PVA (-196°C) aerogel and the corresponding diameter distributions of the micro-pores of the aerogel (f).

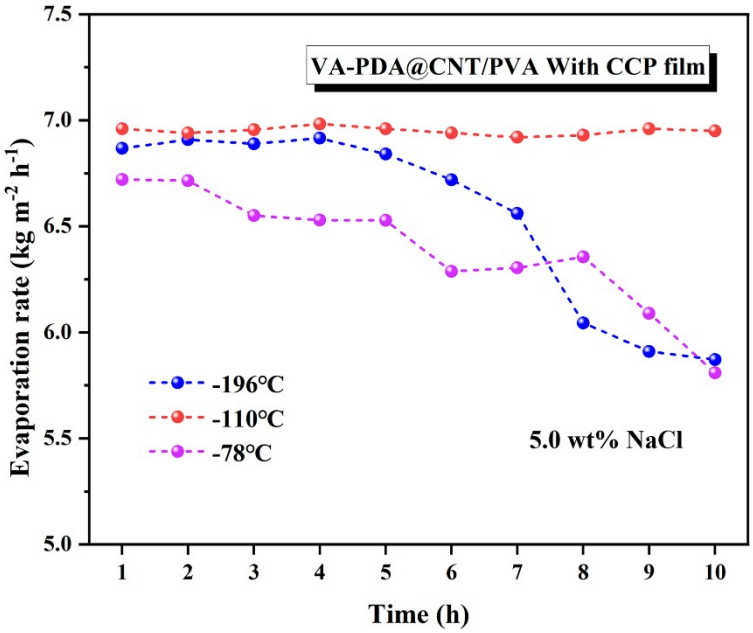

Figure S31 The evaporation rates of VA-PDA@CNT/PVA (-196°C), VA-PDA@CNT/PVA (-110°C) and VA-PDA@CNT/PVA (-78°C) with CCP film evaporators under 1sun irradiation in 5.0 wt% Nacl for 10h

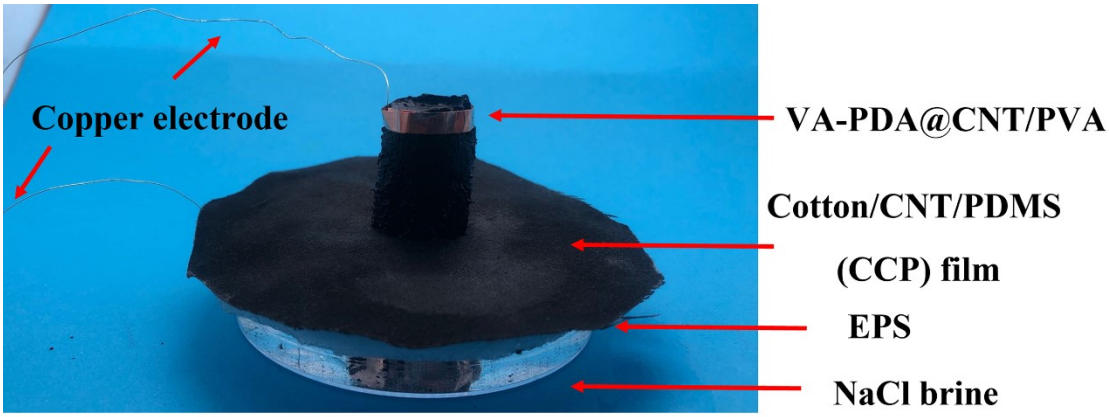

Figure S32 The demonstration of solar evaporation devices

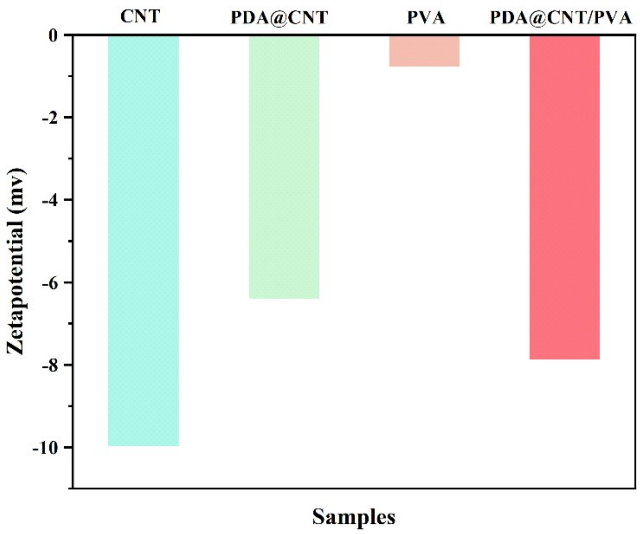

Figure S33 Zetapotential of CNT, PDA@CNT, PVA and PDA@CNT/PVA

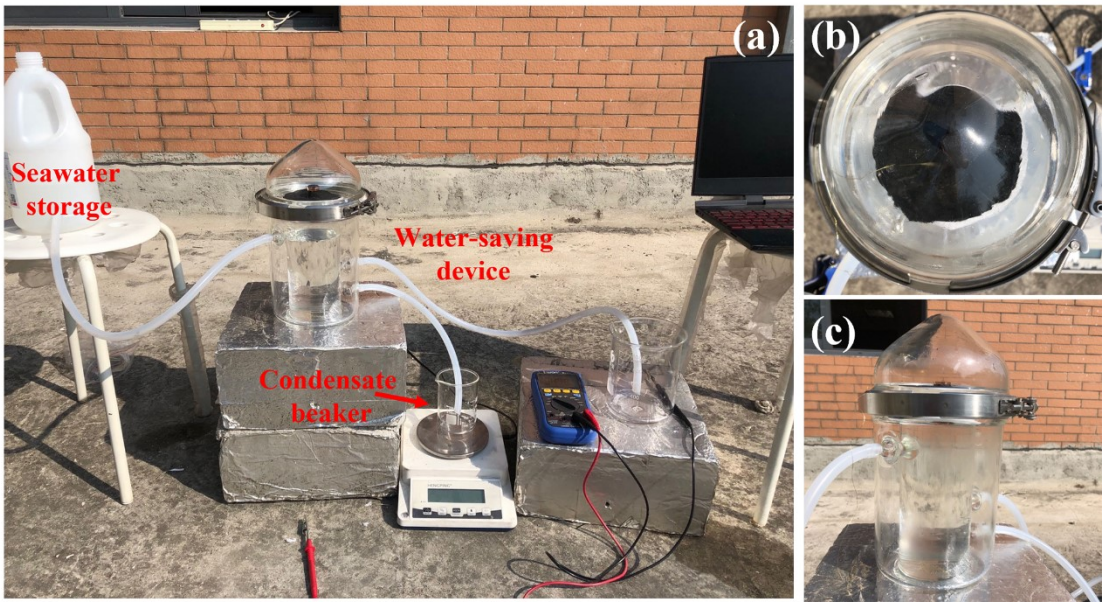

Figure S34 Digital photographs of self-made solar desalination power generation integrated device

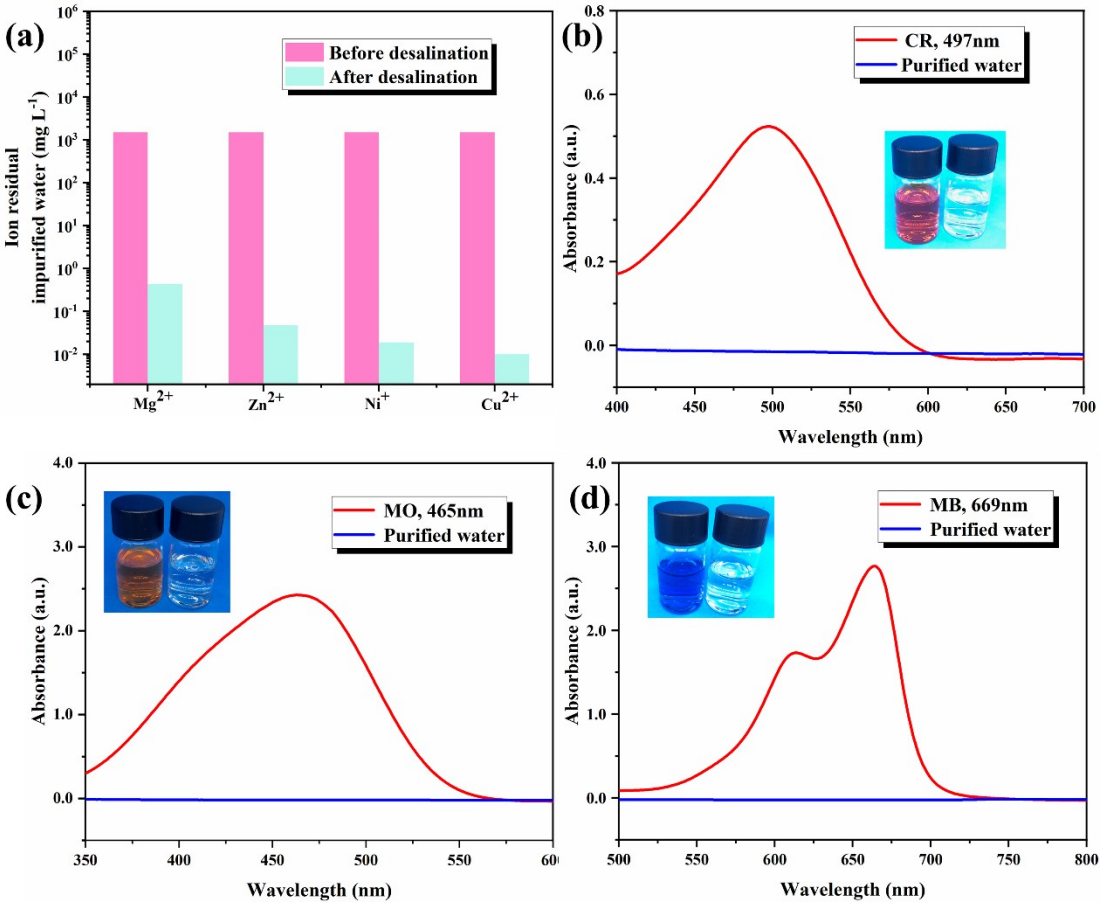

Figure S35 (a) The concentration of heavy metal ions in aqueous solution before and after purification, (b-d) UV absorbance of different dyes before and after purification before and after purification treated by VA-PDA@CNT/PVA with CCP film evaporator.

References

1. Sun, Z.; Han, C.; Gao, S.; Li, Z.; Jing, M.; Yu, H.; Wang, Z., Achieving efficient power generation by designing bioinspired and multi-layered interfacial evaporator. Nat Commun 2022, 13 (1), 5077.

2. Dong, X.; Si, Y.; Chen, C.; Ding, B.; Deng, H., Reed Leaves Inspired Silica Nanofibrous Aerogels with Parallel-Arranged Vessels for Salt-Resistant Solar Desalination. ACS Nano 2021.

3. Xiao, P.; He, J.; Ni, F.; Zhang, C.; Liang, Y.; Zhou, W.; Gu, J.; Xia, J.; Kuo, S.-W.; Chen, T., Exploring interface confined water flow and evaporation enables solar-thermal-electro integration towards clean water and electricity harvest via asymmetric functionalization strategy. Nano Energy 2020, 68.

4. Jia, C.; Li, Y.; Yang, Z.; Chen, G.; Yao, Y.; Jiang, F.; Kuang, Y.; Pastel, G.; Xie, H.; Yang, B.; Das, S.; Hu, L., Rich Mesostructures Derived from Natural Woods for Solar Steam Generation. Joule 2017, 1 (3), 588-599.

5. Mu, P.; Bai, W.; Fan, Y.; Zhang, Z.; Sun, H.; Zhu, Z.; Liang, W.; Li, A., Conductive hollow kapok fiber-PPy monolithic aerogels with excellent mechanical robustness for efficient solar steam generation. Journal of Materials Chemistry A 2019, 7 (16), 9673-9679.

6. Yao, H.; Zhang, P.; Yang, C.; Liao, Q.; Hao, X.; Huang, Y.; Zhang, M.; Wang, X.; Lin, T.; Cheng, H.; Yuan, J.; Qu, L., Janus-interface engineering boosting solar steam towards high-efficiency water collection. Energy & Environmental Science 2021, 14 (10), 5330-5338.

7. Li, L.; He, N.; Jiang, B.; Yu, K.; Zhang, Q.; Zhang, H.; Tang, D.; Song, Y., Highly Salt-Resistant 3D Hydrogel Evaporator for Continuous Solar Desalination via Localized Crystallization. Advanced Functional Materials 2021, 31 (43).

8. Zhao, W.; Gong, H.; Song, Y.; Li, B.; Xu, N.; Min, X.; Liu, G.; Zhu, B.; Zhou, L.; Zhang, X. X.; Zhu, J., Hierarchically Designed Salt-Resistant Solar Evaporator Based on Donnan Effect for Stable and High-Performance Brine Treatment. Advanced Functional Materials 2021, 31 (23).

9. He, S.; Chen, C.; Kuang, Y.; Mi, R.; Liu, Y.; Pei, Y.; Kong, W.; Gan, W.; Xie, H.; Hitz, E.; Jia, C.; Chen, X.; Gong, A.; Liao, J.; Li, J.; Ren, Z. J.; Yang, B.; Das, S.; Hu, L., Nature-inspired salt resistant bimodal porous solar evaporator for efficient and stable water desalination. Energy & Environmental Science 2019, 12 (5), 1558-1567.

10. Liu, P.-F.; Miao, L.; Deng, Z.; Zhou, J.; Su, H.; Sun, L.; Tanemura, S.; Cao, W.; Jiang, F.; Zhao, L.-D., A mimetic transpiration system for record high conversion efficiency in solar steam generator under one-sun. Materials Today Energy 2018, 8, 166-173.

11. Guo, Z.; Zhou, W.; Arshad, N.; Zhang, Z.; Yan, D.; Irshad, M. S.; Yu, L.; Wang, X., Excellent energy capture of hierarchical MoS2 nanosheets coupled with MXene for efficient solar evaporators and thermal packs. Carbon 2022, 186, 19-27.

12. Cao, P.; Zhao, L.; Zhang, J.; Zhang, L.; Yuan, P.; Zhang, Y.; Li, Q., Gradient Heating Effect Modulated by Hydrophobic/Hydrophilic Carbon Nanotube Network Structures for Ultrafast Solar Steam Generation. ACS Applied Materials &

Interfaces 2021, 13 (16), 19109-19116.

13. Wu, L.; Dong, Z.; Cai, Z.; Ganapathy, T.; Fang, N. X.; Li, C.; Yu, C.; Zhang, Y.; Song, Y., Highly efficient three-dimensional solar evaporator for high salinity desalination by localized crystallization. Nat Commun 2020, 11 (1), 521.

14. Gao, C.; Zhu, J.; Li, J.; Zhou, B.; Liu, X.; Chen, Y.; Zhang, Z.; Guo, J., Honeycomb-structured fabric with enhanced photothermal management and site-specific salt crystallization enables sustainable solar steam generation. J Colloid Interface Sci 2022, 619, 322-330.

15. Kong, Y.; Gao, Y.; Sun, Y.; Qi, Y.; Yin, W.; Wang, S.; Yin, F.; Dai, Z.; Gao, B.; Yue, Q., Manipulating a vertical temperature-gradient of Fe@Enteromorpha/graphene aerogel to enhanced solar evaporation and sterilization. Journal of Materials Chemistry A 2022, 10 (7), 3750-3759.

16. Cao, P.; Zhao, L.; Yang, Z.; Yuan, P.; Zhang, Y.; Li, Q., Carbon Nanotube Network-Based Solar-Thermal Water Evaporator and Thermoelectric Module for Electricity Generation. ACS Applied Nano Materials 2021, 4 (9), 8906-8912.

17. Zhou, X.; Zhao, F.; Guo, Y.; Zhang, Y.; Yu, G., A hydrogel-based antifouling solar evaporator for highly efficient water desalination. Energy & Environmental Science 2018, 11 (8), 1985-1992.

18. Sun, Z.; Wang, J.; Wu, Q.; Wang, Z.; Wang, Z.; Sun, J.; Liu, C. J., Plasmon Based Double-Layer Hydrogel Device for a Highly Efficient Solar Vapor Generation. Advanced Functional Materials 2019, 29 (29).

19. Guan, Q. F.; Han, Z. M.; Ling, Z. C.; Yang, H. B.; Yu, S. H., Sustainable

Wood-Based Hierarchical Solar Steam Generator: A Biomimetic Design with Reduced Vaporization Enthalpy of Water. Nano Lett 2020, 20 (8), 5699-5704.

20. He, P.; Hao, L.; Liu, N.; Bai, H.; Niu, R.; Gong, J., Controllable synthesis of sea urchin-like carbon from metal-organic frameworks for advanced solar vapor generators. Chemical Engineering Journal 2021, 423.

21. Liu, N.; Hao, L.; Zhang, B.; Niu, R.; Gong, J.; Tang, T., Rational Design of High-Performance Bilayer Solar Evaporator by Using Waste Polyester-Derived Porous Carbon-Coated Wood. Energy & Environmental Materials 2021, 5 (2), 617-626.

22. Yu, Z.; Gu, R.; Zhang, Y.; Guo, S.; Cheng, S.; Tan, S. C., High-flux flowing interfacial water evaporation under multiple heating sources enabled by a biohybrid hydrogel. Nano Energy 2022, 98.

23. Bai, H.; Liu, N.; Hao, L.; He, P.; Ma, C.; Niu, R.; Gong, J.; Tang, T., Self-Floating Efficient Solar Steam Generators Constructed Using Super-Hydrophilic N,O Dual-Doped Carbon Foams from Waste Polyester. Energy & Environmental Materials 2021, 5 (4), 1204-1213.

24. Xu, X.; Chang, Q.; Xue, C.; Li, N.; Wang, H.; Yang, J.; Hu, S., A carbonized carbon dot-modified starch aerogel for efficient solar-powered water evaporation. Journal of Materials Chemistry A 2022, 10 (21), 11712-11720.

25. Lin, X.; Wang, P.; Hong, R.; Zhu, X.; Liu, Y.; Pan, X.; Qiu, X.; Qin, Y., Fully Lignocellulosic Biomass-Based Double-Layered Porous Hydrogel for Efficient Solar Steam Generation. Advanced Functional Materials 2022, 32 (51).

26. Lu, Y.; Fan, D.; Shen, Z.; Zhang, H.; Xu, H.; Yang, X., Design and

performance boost of a MOF-functionalized-wood solar evaporator through tuning the hydrogen-bonding interactions. Nano Energy 2022, 95.

27. Wang, Z. Y.; Zhu, Y. J.; Chen, Y. Q.; Yu, H. P.; Xiong, Z. C., Bioinspired Aerogel with Vertically Ordered Channels and Low Water Evaporation Enthalpy for High-Efficiency Salt-Rejecting Solar Seawater Desalination and Wastewater Purification. Small 2023, e2206917.

28. Guo, Y.; Zhou, X.; Zhao, F.; Bae, J.; Rosenberger, B.; Yu, G., Synergistic Energy Nanoconfinement and Water Activation in Hydrogels for Efficient Solar Water Desalination. ACS Nano 2019, 13 (7), 7913-7919.

29. Zou, M.; Zhang, Y.; Cai, Z.; Li, C.; Sun, Z.; Yu, C.; Dong, Z.; Wu, L.; Song, Y., 3D Printing a Biomimetic Bridge-Arch Solar Evaporator for Eliminating Salt Accumulation with Desalination and Agricultural Applications. Adv Mater 2021, 33 (34), e2102443.

30. Liu, X.; Tian, Y.; Chen, F.; Caratenuto, A.; DeGiorgis, J. A.; Elsonbaty, M.; Wan, Y.; Ahlgren, R.; Zheng, Y., An Easy-to-Fabricate 2.5D Evaporator for Efficient Solar Desalination. Advanced Functional Materials 2021, 31 (27).

31. Zhu, M.; Li, Y.; Chen, F.; Zhu, X.; Dai, J.; Li, Y.; Yang, Z.; Yan, X.; Song, J.; Wang, Y.; Hitz, E.; Luo, W.; Lu, M.; Yang, B.; Hu, L., Plasmonic Wood for High-Efficiency Solar Steam Generation. Advanced Energy Materials 2018, 8 (4).

32. Ren, H.; Tang, M.; Guan, B.; Wang, K.; Yang, J.; Wang, F.; Wang, M.; Shan, J.; Chen, Z.; Wei, D.; Peng, H.; Liu, Z., Hierarchical Graphene Foam

for Efficient Omnidirectional Solar-Thermal Energy Conversion. Adv Mater 2017, 29 (38).